

**Calibration and performance of the photon-counting detectors for
the Ultraviolet Imaging Telescopes (UVIT) of the Astrosat
observatory¹**

J. Postma

Dept of Physics and Astronomy, University of Calgary, Calgary, AB, Canada

J.B. Hutchings

Herzberg Institute of Astrophysics, 5071 West Saanich Rd., Victoria, B.C. V9E 2E7,
Canada; john.hutchings@nrc.ca

D. Leahy

Dept of Physics and Astronomy, University of Calgary, Calgary, AB, Canada

Received _____; accepted _____

¹Astrosat is an observatory project of the Indian Space Research Organisation (ISRO),
with partnership by the Canadian Space Agency (CSA)

ABSTRACT

We describe calibration data, and discuss performance of the photon-counting flight detectors for the Ultraviolet Imaging Telescopes on the Astrosat observatory. The paper describes dark current, flat field and light-spot images for FUV, NUV, and Visible band detectors at more than one wavelength setting for each. We also report on nominal gain and low-gain operations, full- and sub-window read rates, and non-photon-counting modes of operation, all expected to be used in flight. We derive corrections to the event centroids from the CMOS readout arrays, for different centroid algorithms. We derive spatial resolution values for each detector and plots of point-source signal saturation for different flux levels. We also discuss ways to correct for saturation in extended object images.

Subject headings: Instrumentation: detectors — Space vehicles: instruments — Ultraviolet:general

1. Introduction and data

Astrosat is a multi-wavelength space observatory of the Indian Space Research Organisation (ISRO). The satellite is to be launched in 2012, and contains three pointed X-ray instruments and two UV-optical telescopes, all with fields of view that are aligned. There is also an X-ray scanning sky monitor. The full observatory details and capability are described in the ISRO web pages.

The observatory constitutes a multi-wavelength capability that allows simultaneous monitoring of targets from 100 Kev to optical wavelengths, with high timing precision. It is intended as a facility with proposal time for all, as well as guaranteed time for the instrument teams. Data from all instruments will be available for all observations. The sky monitor will also be a trigger for target of opportunity observations. The mission lifetime is 5 years, which will be extended as long as it remains in good operational order.

The twin UV-optical telescopes (UVIT) have 38cm aperture and field of view of 29 arcmin with roughly 1 arcsec spatial resolution. One telescope has FUV capability and the other covers NUV and blue-optical by means of a beamsplitter. Thus, three wavelength channels are observed simultaneously. Each channel has a filter wheel that contains interference or longpass filters. The UV channels also have gratings, and the optical has a neutral density filter.

The detector details and their basic operational modes are described in Hutchings et al (2009: paper 1), and will not be repeated here. Briefly, the detectors are photon-counting devices, with different photocathodes for each wavelength channel, but otherwise identical. The photocathodes - FUV (CsI), NUV (CsTe), and VIS (S20) - are on the inside of 40mm MgF₂ windows, releasing electrons to be accelerated across a small gap to a microchannel plate stack. The resulting electron cloud illuminates a phosphor, whose light passes through a fibreglass taper, to be read out by a CMOS chip with 512 pixels on a side. Photon events

are centroided to 1/8 pixel to accumulate the final science images. The systems can also be run in ‘integrate’ mode when photon fluxes are too high - principally in the optical channel - which lowers the spatial resolution, but allows centroiding to sufficient precision to track and compensate for spacecraft drift, in accumulating the final UV images. There are three different centroiding algorithms to choose from, and a bright-object shutdown. The full field is read at 29 Hz, but subarrays can be read up to 600 Hz for bright targets or for finer time resolution.

These detectors differ from those flown on FUSE and GALEX in having a readout array of pixels, rather than delay lines (e.g. Morrissey et al 2009, 2011, Sahnou et al 2000). They also differ from the MAMA and delay-line readouts of the STIS and COS detectors (Vallerga et al 2002, McPhate et al 2010). Pixel-based readouts introduce systematic effects in the centroiding and counting of photon events, which require some calibration and testing (paper 1, and Kuin and Rosen 2008, Breeveld et al 2010).

One engineering unit (NUV) and one flight unit for each channel were fabricated by Routes Astro-engineering. Functional tests were performed at the Canadian Space Agency David Florida Lab (DFL), and then were fully tested and calibrated in a specially equipped UV vacuum facility at the University of Calgary. This paper describes the calibration data and their analysis. The paper should be of interest in describing the functionality of the detectors and also for those interested in making observations with the instrument in orbit.

We reported in paper 1 on results from a laboratory version of the photon-counting detector system for the UVIT telescopes. In this paper we describe the calibration and performance of the engineering and flight hardware. The results we describe show the performance of the systems in various modes of operation, and should be useful in designing observing programs with UVIT.

The FUV system has its own flight telescope, and the NUV and VIS share the focal

plane of a second telescope, via a beamsplitter. The 38cm telescopes are designed to deliver images of 1" resolution, but the VIS images will be degraded somewhat by passing through the beamsplitter. Each detector will have filters or gratings on a wheel in the converging beam. All channels will operate simultaneously and have the same (29') field of view. The UV channels are expected to operate mainly as photon-counters, although they all are capable of 'integrate' observations by summing the raw CMOS readout frames. The visible channel is intended mainly for monitoring spacecraft drift by centroiding on a star image using integrate mode, but may also be useful for multi-wavelength observations of variable objects, when used in fast-read photon-counting mode.

The system functional description was given in paper 1. Individual 'front ends' - the windows, MCP, taper, and CMOS readout - were assembled after selection of individual components for engineering, flight, and spares units. Considerations in the selections were the window-MCP gap, which affects spatial resolution, photocathode uniformity and QE, and the cosmetic cleanliness of the optical fibre tapers. The engineering unit had a NUV photocathode and larger than optimal window gap. Each front-end assembly had data from a range of operating gap and MCP gain (voltages) to enable the choice of the optimum values for each. In addition, a number of spatial resolution tests were done on prototype front ends, to characterize the dependence on window voltage and wavelength.

The DFL tests yielded dark frames and pulse-height distributions for detectors at their nominal voltage settings. The event centroiding algorithms built into the flight units are the 3-cross, 3-square, and 5-square subarrays from those described in paper 1. A settable bright-object protection threshold is also built in, which shuts down the high voltage, if it is exceeded in adjacent events in the readout.

The Calgary lab is built about a small, dark vacuum tank, with ports that allow light from lamps with a monochromator. The light flux can be controlled by an aperture, and

the level is monitored by a UV-sensitive photometer through a beamsplitter from the main beam. The light can be collimated, but the collimated beam is smaller than the detector windows, and not very uniform. Uniform illumination for flat fields was available using an integrating sphere within the tank, fed by an uncollimated beam.

Molecular contamination is important to control for UV-sensitive detectors, and the entire lab was kept clean, and entered via an air-shower. Hardware was handled on a clean flow bench. The detectors were mounted in the tank, along with their flight power supplies, on a platform that moves in 3 axes, and were operated by ground support equipment (GSE) outside the tank. Data were viewed and logged via the GSE, and final images were derived later in a separate computer system.

We describe below the different test results and their implications for science use on Astrosat.

2. Darks and read rates

In photon-counting operation, the dark current behaviour is a peripheral concern. But for the UVIT detector system, a quasi-integrate mode feature was also developed, in which it is very important to understand the behaviour of the readout dark current. At nominal gain, a single detected photon event will utilize the maximum amount of CMOS ADC bit depth without saturating the detector in order to maximize counting and centroiding fidelity. Therefore two photons detected in one place within a single read-frame will saturate the CMOS. This is analogous to pulse pile-up on single channel photometers. At normal high-voltage operating parameters, the frames are read at approximately 30Hz for full-frame CMOS scanning (512 x 512 pixels), and up to approximately 600Hz for a sub-scan of 100 x 100 CMOS pixels. Increasing the read rate to 600Hz from 30Hz will allow brighter objects

to be imaged, extending the dynamic range by more than 3 magnitudes.

At all these rates, the background in a single CMOS scan is basically a bias frame, as there is too little time to allow any appreciable build-up of dark current. The local background bias surrounding a photon event is then estimated by the Electronics Unit, and is necessarily corrected for in the calculation of the centroid. In order to mimic an integration-style data collection, we have included an imaging parameter to slow the scan rate of the CMOS by inserting a gap-time (i.e. a delay) between read scans of successive CMOS rows. The result is that when starting an imaging sequence, the first image will have a ramp-up to the total integration time by the end of the last row-read, but successive frames after that will all have equal integration times for each CMOS pixel row. This is not as ideal as integrating the entire frame at once and then reading it all at once, but is quite workable.

The maximum row-gap gives an integration time for the entire frame of about 1.7 seconds (see Table 1). Generally, such integration cannot be done at high gain because the CMOS pixels will saturate almost instantly with most sources. Therefore, a lower gain on the MCP is used in order to reduce the signal level by a factor 10 or more, and therefore allows multiple photons events to fall on one location on the CMOS without saturating the pixel wells. True dark-current then becomes a problem. Dark-current is typically highly dependent upon temperature, but the expected temperature averages of the detector in orbit are expected to be similar to those in the laboratory, typically around 20°C. These measurements were therefore taken in order to examine some typical dark-current characteristics. Table 1 shows the dark current from the three channels for different integrate times. The current is not uniform across the detectors, so we show the range and mean, smoothed over 10 pixels. Table 2 shows the photon-counting read rates for different window sizes.

3. Flat fields

Flat fields were measured using a UV-reflective integrating sphere. The exit aperture of the sphere was 3 inches (significantly larger than the 40mm detector windows), and the detector window was placed directly in front of the aperture at a distance of 1-2 mm. Flat fields were measured for 5x5 Square and 3x3 Square centroiding algorithms, in photon counting mode, and at high and low voltage for each. Aside from photon statistics, at a particular voltage there would not be any expected broad-scale (i.e. larger than 1 pixel) difference between 5x5 or 3x3 algorithms; the important differences should be seen at sub-pixel resolution where fixed-pattern-noise effects are present. There is an expected broad-scale difference between high and low MCP gain (voltage) however, due to areal variations in MCP gain, as can be seen in Fig 1. At low gain, individual photon events on the CMOS are smaller than a readout pixel, so that the centroiding fixed pattern is extreme. We describe this, and its correction, in the following section. The large-scale flat field images are very uniform for nominal gain, but are significantly peaked in the centre at low gain.

4. Fixed pattern noise

There are several factors that affect the accuracy of the sub-pixel part of the centroid, as calculated. The first is because the sampling gradation of the event is so coarse, i.e., it is significantly under-sampled, and this automatically causes the centroid to become systematically less accurate as the event centre lies closer to a pixel boundary. A centroiding ‘box’ of one pixel allows no sub-pixel centroiding; a box of three pixels in one dimension improves upon that significantly, but is still relatively under-sampled, and a sample of 5 only improves slightly because very little energy is deposited in the outer pixels, and noise of various types becomes significant.

A second reason is that a linear centroiding scheme is being used to calculate the centre of a generally Gaussian signal. This also causes a systematic error in the calculation of the centroid. Gaussian centroiding schemes were tested in the initial phase of the Electronics Unit design, and were found to be extremely accurate at centroiding the expected event profiles. However, these schemes require logarithmic calculations and were too slow for the FPGA hardware which was limited in how many cycles were available for each centroid calculation, in order to keep up with the required high data rates.

The third, but possibly not final reason, is that an individual CMOS pixel is not uniformly sensitive across its area - some small areas of a pixel are more sensitive than other areas, and this is also a general systematic effect.

Also, if the source of photons is non-isotropic, meaning that the distribution of photons on the detector face is not "flat", such as an extended source with flux gradients, or a point source convolved with the relevant resolution function, this will also introduce topological effects in the centroid histogram. However, these effects are due to the source, and generally this is the scientific information one desires, and it is also not systemic. The goal of course is to be able to correct for the systemic effects, while leaving the source-topological effects in place. For this reason a flat field source, as provided by the integrating sphere and the resulting images, is used to determine the systemic centroiding effects.

These systematic centroid errors are called Fixed Pattern Noise, or FPN. It would be somewhat more accurate to call it fixed pattern bias. Figure 1 displays the effects of the Fixed Pattern Noise. At nominal MCP gain, the 3x3 algorithm produces a distinct "screen-door" appearance, even though the source was illuminating the detector face evenly. For the 5x5 algorithm the effect is somewhat less, but still apparent. If the average FWHM of the events were only 0.1 pixels or more wider, the 5x5 algorithm performs much better than the 3x3, as shown in paper 1. However, the smaller events sizes result from the

deliberate choice of small window gaps, to yield the best spatial resolution. At low MCP gain, both algorithms perform equally poorly.

The resolution of the photocathode (see following sections), and the resolution of the UVIT telescope are of order 0.4 readout pixels, so the flight science images will be centroided to 0.25 pixels. If we centroid the flat fields to 0.06 pixels or better, we can resolve the MCP pores, as shown in Fig 2. This is of use in that the pore grid can be used as a measure of the centroid error and the correction algorithms.

5. Centroid error corrections

The systematic centroiding bias, or Fixed Pattern Noise, can be corrected for significantly, while leaving the scientific information intact. This is simplest to do for the 3x3 Square centroiding algorithm because a mathematical solution can be programmed which closely mimics the real-world behaviour of the algorithm. In the absence of noise, the 3x3 Square algorithm would always return a centroid with a fractional part which does not fall outside of the maximum-pixel boundary and can be thus corrected. For the 3x3 Square, it is rare for noise effects to skew the centroid outside the boundaries of the maximum pixel, and therefore the noiseless mathematical solution is a decent approximation of the required correction.

The situation is less good for the 5x5 algorithm, since noise effects in the outer pixels with low signal, skew more centroids outside of the central maximum pixel, and therefore a Monte-Carlo style simulation would be required in order to develop a correction algorithm numerically. On the other hand, as we showed in paper 1, the 5x5 algorithm gives better centroids without correction.

The mathematical solution is simply the comparison of a theoretical probability

distribution of centroids, to the real-world probability distribution. If the centroiding accuracy were perfect, then the probability distribution of intra-pixel centroids would simply be a straight line of slope equal to the ratio of the total number of events over the number of sampling bins within a pixel. The corrections need to be performed at a much higher resolution than the physical sampling (1/16th of a pixel), and so the real centroids are redistributed evenly within their 1/16th bins, at 1/1024th pixel resolution. The cumulative sum of this new distribution is its cumulative probability distribution, and this can be divided by the constant-slope line of the theoretical probability distribution to get the correction factor for each 1/1024th bin. In other words, each 1/1024th bin of the interpolated centroid data is multiplied by the correction factor, which is the ratio of the real cumulative probability distribution over the theoretical one. If the real data were composed of centroids from a "flat" illumination of photons, then the systematic centroiding bias effects will have been corrected for. This flat-field correction curve can then be applied to data which has sources and other topological variations - i.e. valuable scientific information, and the correction will only apply to the existing systematic bias within the data, but leave the source-topological variations undisturbed.

Paper 1 gives more detailed description of the corrections, and shows how the signal is redistributed within a pixel. Essentially, the distribution is remapped by performing a division by the correction factor. All photons are conserved, so no photometric error is introduced.

The fraction of out-of-pixel centroids depends to some extent on the size of the photon event on the CMOS readout. For our flight detectors, with the 3x3 Square algorithm, there are approximately 1-2% of centroids which fall outside of the central pixel boundary, and therefore these will not be adjusted to the correct position and will thus constitute noise. For the 5x5 Square algorithm, the fraction is approximately 5-7%. However, it should be

pointed out that the reason these centroids were outside of the pixel boundary in the first place was because of a noise skew, and so the correction scheme doesn't actually introduce more noise, but rather simply conserves it.

Figures 2 and 3 show parts of flat-field images with 3x3 centroiding before and after correction. The final science images will have the 1/4 pixel resolution of Figure 2. A final point to note is that in flight, there will be spacecraft jitter of amplitude a pixel or more over the time of an observation. This will be monitored by guide-star centroids from the VIS channel and the photon centroids corrected in building up the science image. The effect of this will be to smooth out the FPN, so that it may be a matter of post-observation observer choice whether the corrections are needed in a given image.

6. Hole mask data

Spatial resolution and flux calibration were performed using the hole mask (see Fig 4). These holes are all 25 microns in diameter, to an accuracy of 5%. The mask was taped close to the detector face, about 1mm from the window, and illuminated with the collimated beam. There are two points to note in this. First, the beam illumination underfills the detector window, and is not uniform. Second, the mask is a small distance from the photocathode, by the window thickness and the gap between the window flange and its outer surface, so the spots are somewhat enlarged by diffraction.

We used the first point to our advantage by the fact that the spot images cover a wide range of signal levels, thus increasing the dynamic range of the flux calibration. The response uniformity across the detector window was checked by using a range of flux levels, and by moving the detector around the collimated beam.

We calibrated the second point by using results from a different hole mask used in

testing the engineering model detector. This mask had alternating hole sizes of 25, 50, and 75 microns across its diameter. The actual spot image sizes are shown in Fig 5. Given the very linear relationship, it is evident that the diffraction and spot size effectively add, and we have used the extrapolation to zero hole size as a measure of the detector resolution, as shown in the diagram. The measured spot sizes for the 25 micron hole mask data were similar to that in Fig 5. The same slope and extrapolation was therefore applied to the image size measured with the 25 micron hole-mask used with the flight detectors. There was insufficient calibration time to get images with the multi-sized hole-mask with the flight detectors, but the geometry and window thickness was the same for all detectors, so Fig 5 was applied to all cases. In the next section, we note other ways to make this measure, and their good agreement.

Spot sizes are defined as the FWHM values from the images. These are expressed in readout pixels, and can be converted to values at the photocathode or arcseconds on the sky as seen with the UVIT telescope. Signal levels were integrated over the final spot images.

7. Spatial resolution

The spatial resolution was also estimated by the images of the cross-shaped hole arrays with differently spaced separations. These arrays were oriented at several different angles, to allow different sampling by the readout pixel array. Figure 6 shows some of these images, not corrected for centroiding systematics, and Fig 7 shows plots from summing pixel rows across one of the cross arms.

The smallest spot separation is 30 microns, centre to centre, so the smallest gap between them is 5 microns. The next smallest gap is 20 microns. The resolution is different for the 3 detectors, as expected from their window gaps and the photon wavelengths (see

figs 7 and 8), but in all cases the 20 micron gap is well resolved, and the 5 micron gap is not.

The resolution estimates by both methods agreed well, and table 3 shows the adopted average numbers for the spatial resolution for the 3 detectors. The wavelengths used, and the photocathode gaps are also shown. The ‘predict’ numbers are the values expected from the front-end tube measures. Figure 8 shows these and the dependence of resolution on wavelength and gap, and compares the front-end tube tests before assembly with the final values from the fully integrated detectors. The numbers ‘corrected to sky’ give our estimates of FWHM in arcseconds on the sky. The values are much as expected, except for the visible wavelength detector, which is about twice the expected value. The longer wavelengths of the VIS channel will cause more diffraction through the mask apertures but will not explain this amount of difference. The scientific impact is small, however, as the telescope optical resolution is poor because of passing through a beamsplitter. The main use of the optical channel is for tracking spacecraft drift via star centroids, and there will be no impact on this performance, since the much larger integrate mode images will be used.

We note also that the resolution as measured from images with low MCP gain is very similar. The percentage numbers given for these are the signal reduction when using low gain, as it is intended for use with bright stars which would cause detector damage at full gain.

In Figure 9, we illustrate the resolution in the case of two closely spaced point source images. The profile is approximated by a gaussian, but an average spot image is shown, and has a slightly narrower peak and some weak broad wings. The plot shows how the profile is significantly broadened with a separation of only some $0.3''$, and shows separate peaks when separated by about $0.8''$.

These results indicate that the UV detectors will yield image resolutions of 1 arcsec

or better, and the visible channel a little larger. The ultimate resolution of the UVIT instrument will combine these with the optical resolution of the telescope and the drift of the spacecraft during observations. The telescope should deliver images of 1 arcsec FWHM, and we expect to correct drift using the visible channel guide-star centroids, to a small fraction of that.

Figure 10 compares the integrate mode images (simply the sum of all the photon event splashes) with the centroided image resolution we report above. Integrate mode images can be centroided to 0.1 pixels, or 0.25 arcsec, to compensate for spacecraft drift.

8. Flux calibration

The flux calibrations used the same hole-mask data. The wavelength was selected with the monochromator, and the flux monitored by photometer readings from a beam-splitter. A series of (usually four) flux settings was used for all images. Data were taken in photon-counting mode with 5S and 3S centroiding, and Integrate mode, and with full frame (29Hz) and a subwindow (293Hz) readout. Images were accumulated for all these settings, and their relative count rates logged by measuring the event counts per second (not per frame) of the same (brightest) spot. The sub-arrays were chosen to cover a region well-filled with measurable spots. In any images, there are spots covering a wide range (about a factor 5) of signal levels. The spots are small and well-separated, so no crowded field issues arise, and they simulate star images in a sparse field. Having established that there is no wavelength dependence of signal saturation, one wavelength was selected for this work for each channel. In addition, all data were taken at nominal and low gain.

In any one image, about 6-10 spots were measured, covering the full range of signals. The same spots were measured for all four flux settings. The signals were measured using the

‘rimexam’ task within IRAF, using radii selected for the spots for object and surrounding background. The same measurement settings were used for all spots and channels. The measurement radius was 5 pixels, and the sky an annulus between radii 7 and 9 pixels. The signal levels were accumulated in a table for all spots and flux settings.

The saturation plots (Fig 11) were generated as follows. Signal level is plotted against photometer flux reading for the brightest spot measured. The flux levels of the fainter spots were scaled by the ratio of the signal levels for the lowest two flux settings, compared with that for the brightest spot. In all cases the signals were not saturated for the lowest two fluxes, so this scaling should be good. This leads to points that cover the range of flux and signal quite well. In the case of the subarrays, the number of spots was more limited, so that it was sometimes not possible to cover the ranges as well as we wished.

Figure 12 shows an EM NUV channel saturation plot, derived from the mask with different-sized holes. The saturation curve is different from those of the flight systems because of the different event size and poorer resolution of this detector, illustrating how individual each system is. Figure 12 also shows the flux calibration for VIS channel integrate mode images, whose effective integration time is set by the time gap between pixel row reads (row gap). This low gain INT mode operation is expected to be the default for the VIS channel when used for drift monitoring on bright guide stars.

There are similar results for the NUV spot signals with low gain setting. For all low gain operations, we note that the flat fields show large variations in signal from centre to edge of the field, so that flux calibrations will be reliable only for objects in the central part. In addition, low gain is intended for cases where there are bright objects giving high count rates. We can adopt low event thresholds to account for the lower gain, but this allows noise to be included in the accepted data. The result of these considerations is that the calibration plots, shown below, show significant scatter and non-linear response at low

signal levels. Nevertheless, they are useful in allowing observations of bright targets, which should be placed at the centre of the field and read with a small subarray.

So far, we have used only signal levels in counts from the images as described, and flux levels as measured in arbitrary units on our photometer, via a beamsplitter. In order to convert signal levels to photons at the photocathode, we need to apply a factor that measures the absolute QE of the systems. This was done by using a NIST calibrated diode in the beam, and the results are shown in Figure 13. This way we can convert from source counts to incident photons. To plan observations through the entire telescope we need to include an extra factor for the telescope optics and filter throughputs as well. These will be published and updated on the proposal website for the mission, once established.

The absolute QE of the FUV detector at the wavelength of observation (150nm) is measured at close to 3%. This gives a conversion from the source total signal in the plots to photons at the photocathode of 0.77. That is, we multiply the source counts by 0.77 to get the incident photon counts. The NUV wavelength used was 210nm, at which the QE is close to 10%, and the QE for the visible is also close to 10%. This gives a conversion factor from plotted source signal to photons of 0.37 for these channels.

9. Detection of double-photon events

As noted in paper 1, double-photon events can be flagged by using the max-min corner pixel values from the 5 x 5 events boxes. It is these events that lead to the non-linearity and saturation plots shown. We performed some double-photon rejections based on various values of the rejection threshold, to check whether saturation leads to degradation of the spatial resolution.

The reader is referred to paper 1 for the detailed description of this rejection process,

but we give a brief summary here. Double-photon events statistically lead to broader events patterns in the readout image, and they can be isolated by the difference between the maximum and minimum pixels signals in the 5x5 event box. Each detector has an optimum value of this threshold, depending on the individual event sizes and the intrinsic spatial resolution of the device. Using ‘no rejection’ accepts all events, while a high rejection threshold will identify only the most egregious of double-events.

In the case of single isolated spots (i.e. stars in real observations), there is no significant change to the point source resolution if we reject such events. Thus, we do not need to apply such thresholds for science images to resolve stars. This is true for images of two closely spaced spots (stars).

Figure 7 of the paper by Srivastava, Prabhudesai, and Tandon (2009), points out how flux can be lost from bright crowded regions of extended images with structure. To look for this, we inspected the close-spaced cross of spots in our images with a range of count rates. This will show up as spots in the centre of the pattern having less signal than the outer (less crowded) ones, since the spots imaged all in fact have the same flux. In general, we don’t see any effect for the lower three flux values, but it does show up in the highly saturated images.

This is potentially a problem for science analysis, but can be alleviated by identifying the double events in the image, and adding them back in again, so they get counted twice, as they should be, instead of only once. In principle, triple events can be treated in the same way by setting a different (lower) max-min threshold, but this is less reliable as it is more susceptible to random noise too. Figure 14 shows an example of this correction in one close array of spots, where saturation is clearly present in the crowded inner parts of the image. Table 4 shows the flux corrections at two different flux levels, for isolated spots, the end spots of the cross-grid, and the entire cross-grid. The values are shown for a range

of rejection threshold values. Isolated spots show no signal loss at the low flux value, while at high flux, they do - more markedly for the brighter spot, as would be expected. The cross-grids behave in many ways like an extended object with structure, and signal loss (double events) are seen even in the outer spots. The signal loss of the entire grid is seen at both flux values. The table also gives the restored flux from compensating for the double events by counting them twice. It is clear that this process will be needed to analyze bright extended images.

We thank Routes Asto-engineering, particularly Don Asquin and Josee Cayer for their work on the hardware and its initial testing. We also thank Shyam Tandon for his active participation, and discussion of the results presented here. We thank the referee for useful comments on our presentation. We thank the Canadian Space Agency for support.

References

Breeveld A. A., et al, 2010, MNRAS, 406, 1687

Hutchings, J.B., Postma J., Asquin D., Leahy D., 2007, PASP, 119, 1152

Kuin N.P.M., and Rosen S.R., 2008, MNRAS, 383, 383

McPhate J., et al, 2010, Proc SPIE 7732, 2H

Morrissey P., et al 2009, ApJS, 173, 682

Morrissey P., et al 2005, ApJ, 619, L7

Srivastava M.K., Prabhudesai S.M., Tandon S.N., 2009, PASP, 121, 621

Vallerga J, et al 2002, Nucl Instrum Meth A 477, 551

Captions to figures

1) FUV detector flat field images with 3x3 centroiding at 1/8 pixel resolution: 8x8 pixel subarray detail at the top and full images on the bottom. The left side images are with nominal gain and the right side are at low gain.

2) NUV flat field detail with 1/32 pixel resolution, in which the MCP pores can be seen. The centroids are from 3x3 subarrays. The right panel shows the raw image, which shows the pixel boundary effects clearly. The left image has been corrected and removes most of the errors.

3) NUV channel 3x3 centroid detail at 1/8 pixel resolution. The left panel is the raw image and the right panel has centroid corrections applied.

4) Details of hole mask used for flight system flux and resolution measurements. The holes are all 25 microns in diameter. The cross-shaped arrays have different orientations to sample the readout pixel array differently.

5) Measured EM spot image FWHM from a hole mask with 25, 50 and 75 micron holes. The numbers in parentheses are the actual image FWHM at the photocathode, broadened by diffraction between the mask and the photocathode. The system spatial resolution is defined as the size of the detected image from the linear fit extrapolated to zero size. See text for discussion.

6) Some typical 3x3-centroid images of the spot array in different orientations. The readout pixel edges are clearly seen.

7) Plots of signal from rows summed along the arms of the spot array, with detectors at wavelengths noted. The smallest separation is 30 microns. The profiles are slightly confused near the centre where they cross, and by pixel boundaries in the individual spot images. The 180nm image is the dotted line, and has the highest resolution (see Table 3).

8) The measured image FWHM in microns at the photocathodes. The angular scale on the sky is shown on the right. The lines are derived from ‘front-end’ only resolution measures made on prototype tubes. The tube resolution depends on the wavelength (photoelectron energy), and the gap between the photocathode and the MCP surface. The filled squares show the measured flight system values, and the open square is the NUV engineering model. The final system resolutions are close to expectation except for the VIS channel.

9) Plots showing the profile from two calculated images represented by Gaussians of FWHM $0.8''$, shown as the dark solid line. The actual image profile for the FUV detector is the dotted line, which is slightly narrower at the peak, but with some outer wings. Thus, the model is a good representation. Significant profile broadening is seen at $0.3''$ separation and the peaks are separated at $0.8''$ separation.

10) Comparison of the same spots imaged in photon-counting mode (left) and in integrate mode (right). The photon-counting images are about $1''$ on the sky and the integrate mode images are many times broader (FWHM $\sim 10''$ on the sky). However, the integrate mode images can be centroided to $0.2''$ or better to correct spacecraft drift at that level. in building up the photon-counting images.

11) Flux calibration of FUV detector, comparing saturation effects between slow and fast read, and normal and low gain operation. In the top two panels, dots are from high gain and circles from low gain. Dotted lines indicate the non-linear saturation effects. Rapid read subarrays allow a alrger dynamic range before saturation becomes severe. Low gain reduces the signal levels by factors two or more. The text in section 8 describes the units and their conversion to photons.

12) Upper: saturation for the EM detector. Signals are in units of 1000 counts. The different symbols refer to small and large hole spots on the same mask, scaled by their

relative throughput. Lower: Flux calibration for the VIS channel detector with integration time (row gap), for two different flux levels. Both are in the low MCP gain mode.

13) QE of the three detectors with wavelength.

14) 3-d representation of spot array image at high flux level. The spots all have the same brightness. Double events in the crowded central area reduce the inner spot signals (top). The middle panel shows how many single events are present. The lower panel shows the restored flux image from adding back the double events to the image. The lines across the peaks are to guide the eye.

Table 1. Dark current values in electrons per read

| Row | Read | FUV | | | NUV | | | VIS | | |
|-----------|----------|------|------|------|------|------|------|------|------|------|
| gap | interval | Min | Max | Mean | Min | Max | Mean | Min | Max | Mean |
| 0.0033sec | Sec | | | | | | | | | |
| 0 | 0.035 | 1339 | 1595 | 1390 | 1442 | 1727 | 1497 | 1447 | 1733 | 1512 |
| 63 | 0.241 | 1305 | 2577 | 1362 | 1398 | 2641 | 1451 | 1420 | 2826 | 1488 |
| 127 | 0.451 | 1308 | 3438 | 1373 | 1375 | 3441 | 1444 | 1423 | 3788 | 1504 |
| 191 | 0.661 | 1307 | 4133 | 1395 | 1368 | 4122 | 1455 | 1423 | 4569 | 1528 |
| 255 | 0.870 | 1307 | 4705 | 1424 | 1366 | 4723 | 1477 | 1427 | 5244 | 1561 |
| 319 | 1.080 | 1311 | 5198 | 1460 | 1371 | 5232 | 1505 | 1432 | 5817 | 1598 |
| 383 | 1.290 | 1318 | 5624 | 1501 | 1377 | 5636 | 1542 | 1437 | 6315 | 1640 |
| 447 | 1.500 | 1322 | 5988 | 1546 | 1385 | 5913 | 1582 | 1446 | 6757 | 1685 |
| 511 | 1.709 | 1330 | 6289 | 1594 | 1392 | 6253 | 1625 | 1456 | 7150 | 1733 |

Table 2. Read rates for
different subwindow sizes

| Width | Height | Hz |
|-------|--------|------|
| 512 | 512 | 28.7 |
| 409 | 409 | 44.3 |
| 306 | 306 | 77.3 |
| 203 | 203 | 168 |
| 100 | 100 | 605 |
| 512 | 100 | 147 |
| 100 | 512 | 118 |

Table 3. Spatial resolution summary

| Property | FUV | | NUV | | VIS | EM |
|---------------------------|-------|-------|-------|-------|-------|-------|
| | 180nm | 150nm | 125nm | 210nm | 400nm | 230nm |
| Gap (μ) | 110 | 110 | 110 | 100 | 140 | 170 |
| Event size (px) | 0.92 | 0.92 | 0.92 | 1.18 | 1.16 | 1.30 |
| Image FWHM (px) | 0.35 | | 0.45 | 0.38 | 0.60 | 0.55 |
| Expected ¹ | 0.8" | | 1.1" | 0.7" | 0.7" | 1.1" |
| FWHM on sky | 0.8" | | 1.0" | 0.9" | 1.3" | 1.2" |
| Low gain | | | | | | |
| Signal level ² | | 10.5% | | 8.6% | 4.8% | |
| FWHM (px) | | 0.34 | | 0.35 | 0.53 | |

¹From the lines in Figure 8

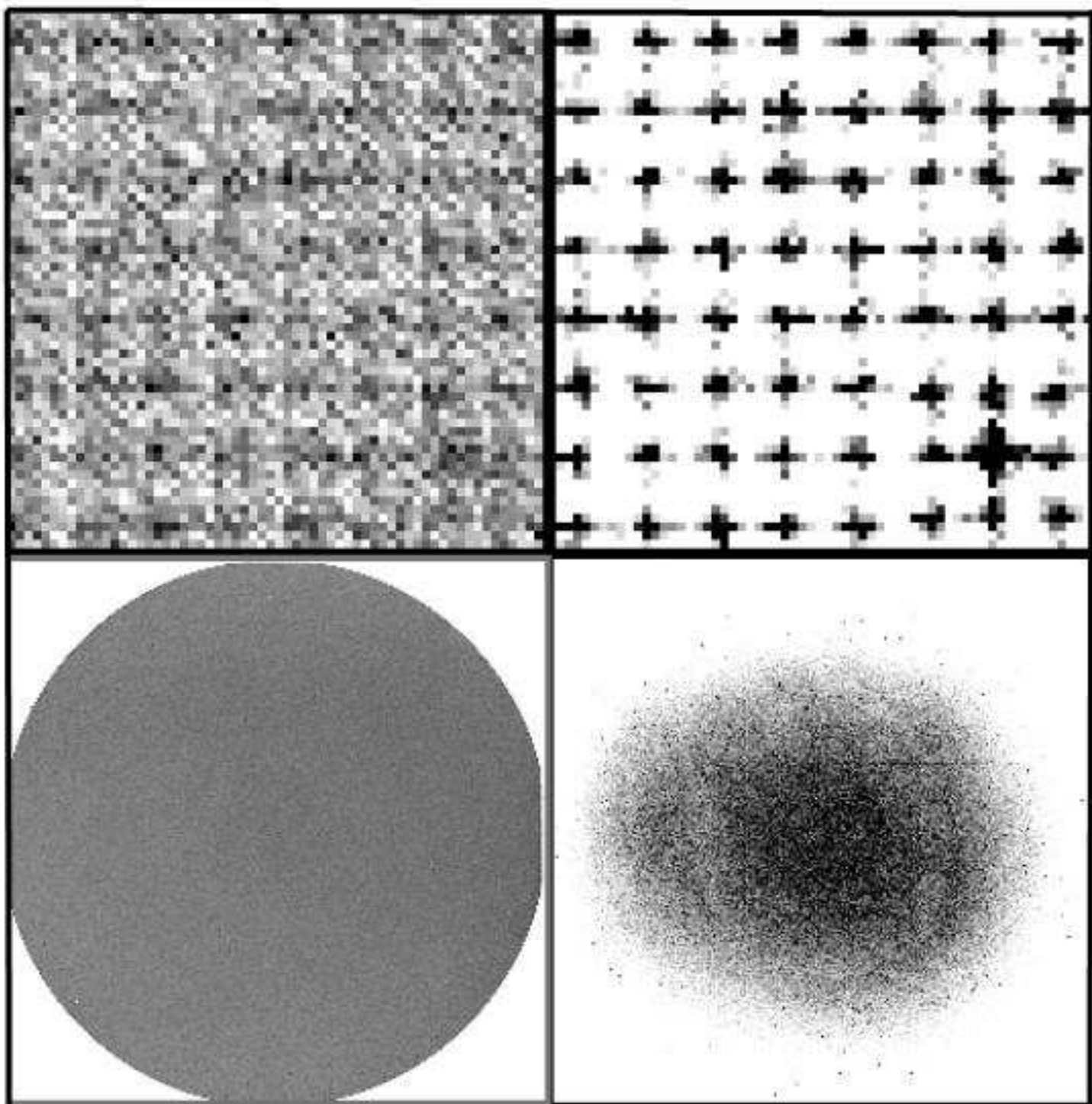
²Signal level reduction from nominal gain

Table 4. Source counts in images with double-events¹

| Rejection threshold | Spot1 | Spot2 | End spot | Cross-grid Whole pattern |
|------------------------|---------------------------------------|-------|----------|-----------------------------|
| | Medium flux = 0.66 events/read | | | |
| None | 794 | 1476 | 534 | 11161 |
| 128 | 797 | 1459 | 536 | 7781 |
| 64 | 811 | 1446 | 450 | 7126 |
| 16 | 766 | 1343 | 269 | 4562 |
| Restored ² | | | 608 | 12785 |
| | High flux = 1.04 events/read | | | |
| None | 2838 | 4996 | 2106 | 35820 |
| 128 | 2739 | 4590 | 815 | 6877 |
| 64 | 2657 | 4165 | 512 | 4330 |
| 16 | 2369 | 2724 | 46 | 1061 |
| Restored ² | | | 3419 | 64765 |

¹See text for detailed explanation

²Restored image signal by counting double events twice



The first part of the document discusses the importance of maintaining accurate records of all transactions. It emphasizes that proper record-keeping is essential for ensuring the integrity and reliability of financial data. This section also covers the various methods used to collect and analyze data, highlighting the need for consistency and transparency in the reporting process.

The second part of the document focuses on the challenges faced by organizations in implementing effective data management practices. It identifies key areas such as data security, privacy, and access control, and provides practical advice on how to address these issues. The text also discusses the role of technology in enhancing data management efficiency and the importance of regular audits to ensure compliance with relevant regulations.

The final part of the document concludes with a summary of the key findings and recommendations. It reiterates the importance of a proactive approach to data management and encourages organizations to continuously monitor and improve their practices. The document also includes a list of references and a glossary of terms for clarity.

The second part of the document discusses the importance of maintaining accurate records of all transactions. It emphasizes that proper record-keeping is essential for ensuring the integrity and reliability of financial data. This section also covers the various methods used to collect and analyze data, highlighting the need for consistency and transparency in the reporting process.

The third part of the document focuses on the challenges faced by organizations in implementing effective data management practices. It identifies key areas such as data security, privacy, and access control, and provides practical advice on how to address these issues. The text also discusses the role of technology in enhancing data management efficiency and the importance of regular audits to ensure compliance with relevant regulations.

The final part of the document concludes with a summary of the key findings and recommendations. It reiterates the importance of a proactive approach to data management and encourages organizations to continuously monitor and improve their practices. The document also includes a list of references and a glossary of terms for clarity.

